Experimental investigation of the gas-liquid interface and flow field dynamics near the contact line in an immersing flat surface

Damien Rigutto[1,2,*], Yannick Lecomte[1,3], Jean-Marie Buchlin[1], Benoit Scheid[2] and Miguel Alfonso Mendez[1]

1: Environmental and Applied Fluid Dynamics, von Karman Institute for Fluid Dynamics, Waterloosesteenweg 72, Sint-Genesius-Rode,1640,Belgium
2: Transferts, Interfaces Et Procédés (TIPs), Université Libre de Bruxelles, Av. Franklin Roosevelt 50, Brussels, 1050, Belgium
3: Université Libre de Bruxelles, Av. Franklin Roosevelt 50, Brussels, 1050, Belgium

*Corresponding author: damien.rigutto@vki.ac.be

Keywords: Gas-Liquid interfaces, dynamic wetting, LIF-based interface tracking, PTV, RBF, POD.

ABSTRACT

Dynamic wetting is fundamental to many coating processes. In hot dip galvanization, an unstable contact line can generate wetting defects and air entrainment in the coating, limiting the quality of the final product. While the literature focuses mainly on capillary-viscous flows, which are amenable to analytical treatment, some configurations, such as dip coating, operate in inertia-dominated conditions. This work presents an extensive and unprecedented experimental characterization of the interface and contact line dynamics on a surface entering a liquid bath in inertia-dominated conditions using laser-induced fluorescence (LIF). Moreover, we complement the analysis with particle tracking velocimetry (PTV) underneath the gas-liquid interface to study the interaction between the liquid flow and the free surface. Proper orthogonal decomposition (POD) of the interface displacement is presented and analyzed in combination with the velocity field dynamics, enhanced by physics-constrained Radial Basis Functions (RBFs).

1. Introduction

The theory of dynamic wetting describes the phenomena occurring when a gas-liquid interface is in relative motion with respect to a solid. The line where the interface meets the solid and sets the boundary between wet and dry regions is known as the “contact line”. The region near the contact line is subject to intense molecular interaction and challenges traditional fluid dynamics based on the continuum hypothesis. A well-known paradox is the contradiction of having "no slip" between liquid and solid while still having a relative motion between the contact line and solid wall (Bormashenko, 2013; Zhao, 2014; Fricke & Bothe, 2020).

A classic configuration featuring dynamic wetting problems is the motion of a substrate withdrawn from or immersed in a bath. Both cases are fundamental in many coating processes (Kistler & Schweizer, 1997). In static conditions, this configuration is widely used to measure surface

tension in the Wilhelmy plate method (Mohammad Karim & Kavehpour, 2018). In dynamic conditions, the withdrawal of the plate sets the basis for the well-known Landau-Levich problem, which aims at predicting how much liquid is entrained with the substrate (Landau & Levich, 1988; Quéré, 1999; Fuentes & Cerro, 2005; Snoeijer et al., 2008; Mayer & Krechetnikov, 2012).

Much less investigated is the immersion problem, where the substrate enters the bath at a certain velocity. Although the first theoretical modeling attempts of this configuration date back to the seminal works of Huh & Scriven (1971), experimental investigations of this configuration are rare and generally limited to highly viscous configurations (Dussan V. et al., 1991; Ramé & Garoff, 1996; Chen et al., 1997; Gupta et al., 2023). To the best of our knowledge, the only investigations that considered inertia-dominated conditions have focused on the problem of air entertainment (Burley & Kennedy, 1976; Benkreira, 2004).

In this work, we aim to fill this gap by investigating dynamic wetting in a high-speed immersing configuration. We use a combination of laser-induced fluorescence (LIF) with image processing and particle tracking velocimetry (PTV) to simultaneously capture the interface shape and the velocity field respectively. The dynamic of each is analyzed and combined in the data treatment. The investigation is extended using proper orthogonal decomposition (POD) to analyze the patterns of the interface dynamics and data assimilation using radial basis functions (RBFs) to enhance the velocity field resolution (Sperotto et al., 2024).

The experiments were carried out in a rotating cylinder facility similar to Fell et al. (2011), but at a considerably higher substrate velocity. We use dimensionless analysis to relate the investigated configuration to various regimes and relevant industrial configurations, namely the hot dip galvanizing. Measuring the dominance of the inertia in terms of Weber number, the wetting conditions are comparable to what is observed in "impacting droplet" experiments, where a droplet hits a plate at a large velocity (order of m/s) (Mitra & Evans, 2018; Quetzeri-Santiago et al., 2019).

The rest of the article is structured as follows. Section 2 presents the scaling analysis and the relevant dimensionless number, whereas section 3 presents the experimental methodology, including the experimental setup, measurement technique, and data processing. The results are presented and discussed in section 4, while the conclusions are drawn in section 5.

2. Investigated conditions and scaling laws

Figure 1a illustrates the configuration considered in this work along with the relevant parameters. A solid and flat substrate enters a bath at a velocity u_p, with an inclination angle θ_e. The liquid is characterized by a density ρ and dynamic viscosity μ, while the gas-liquid interface is characterized by a surface tension σ. The dynamic viscosity and density of the gas are small compared to those of the liquid, which is why we neglect them for the following analysis. The interface meets the

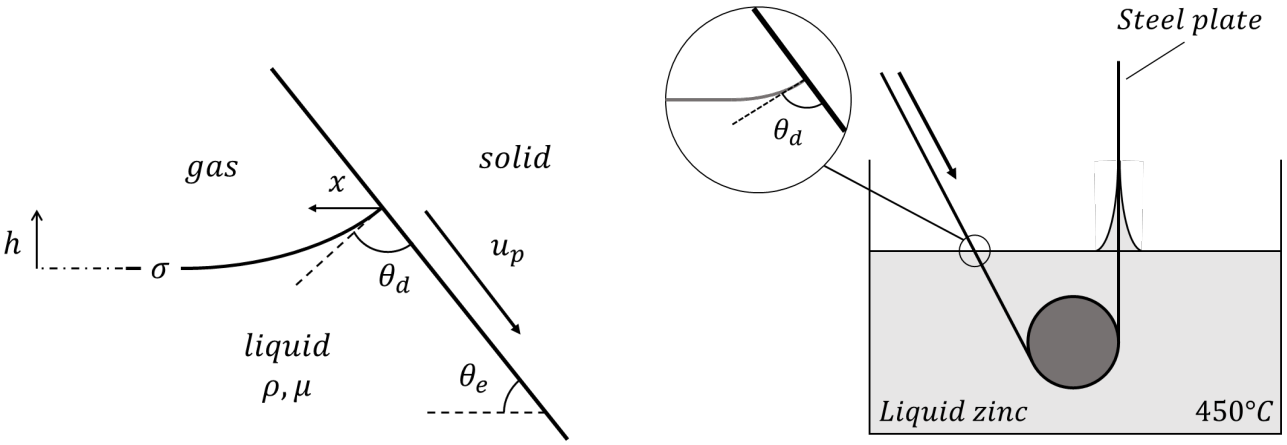

(a) (b)

Figure 1. (a) Schematic of the investigated configuration and main parameters (b) Configuration of interest presented in the industrial context of hot dip coating.

solid with an angle θ_d referred to as dynamic contact angle.

This configuration is encountered in hot dip galvanizing, as sketched in Figure 1b. Here the substrate is a steel strip that needs to be coated and the liquid is a bath of molten zinc at approximately $450\,^{\circ}\mathrm{C}$. Upon solidification, the coating protects the zinc from corrosion. Due to interface instabilities, roughness and local defects on the steel strip, the contact line can undergo rapid accelerations, which could result in air inclusion. When this occurs, localized wetting defects might arise.

In this work, we are interested in investigating how the interface and the velocity field are affected by the substrate entering velocity u_p. The interface elevation h is defined as a function of the distance from the triple point x and the time t. A scaling analysis reveals that the problem can be scaled using three dimensionless numbers. For convenience, we consider the following ones:

$$\frac{h}{l_c}\left(\frac{x}{l_c}, \frac{u_p t}{l_c}\right) = f\left(\mathrm{We}, \mathrm{Ca}, \theta_s\right) \quad \text{with} \quad \mathrm{We} = \frac{\rho u_p^2 l_c}{\sigma}\,, \quad \mathrm{Ca} = \frac{u_p \mu}{\sigma}\,, \quad \cos\theta_s = \frac{\sigma_{SG} - \sigma_{SL}}{\sigma}\,. \tag{1}$$

Having introduced $l_c = \sqrt{\sigma/(\rho g)}$ the capillary length as the reference length, with g the gravitational acceleration and l_c/u_p as the characteristic time. The dimensionless numbers are the Weber number We, the Capillary number Ca and the static contact angle θ_s, which depends on the solid-gas interface tension σ_{SG} and the solid-liquid interface tension σ_{SL}.

The experiments in this work were carried out using water as a liquid and stainless steel as a solid substrate in the MINERVA facility at the von Karman Institute (VKI) which is described in the following section. Figure 2 reports on the conditions explored in this study (○) compared to the inertial conditions encountered in the galvanizing line (□). The static contact angle in the reference conditions is about 22.5° while an angle of 64 ° is obtained for the experimental conditions.

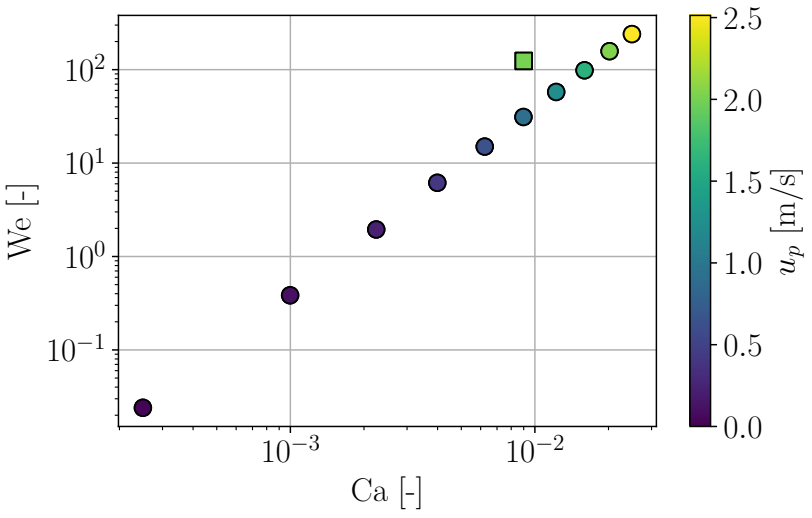

Figure 2. Comparison between the conditions of galvanization (□) and the conditions explored in this work (○), in terms of Capillary (Ca) and Weber (We) numbers, with an indication of the associated entering velocity u_p.

3. Methodology

3.1. Setup and measurement techniques

The MINERVA facility at the VKI is illustrated in Figure 3a. The motion of the entering plate is reproduced using a cylinder made of stainless steel (1) with a diameter of 60 cm. This facility generates substrate velocities up to 3 $\mathrm{m/s}$. The entering angle θ_e can be adjusted by changing the water level in the bath. A PID controller ensures the DC motor (2) gives a precise velocity while a scrapper (4) coupled to an air jet (5), ensures the cylinder is dry before entering the interface at (3).

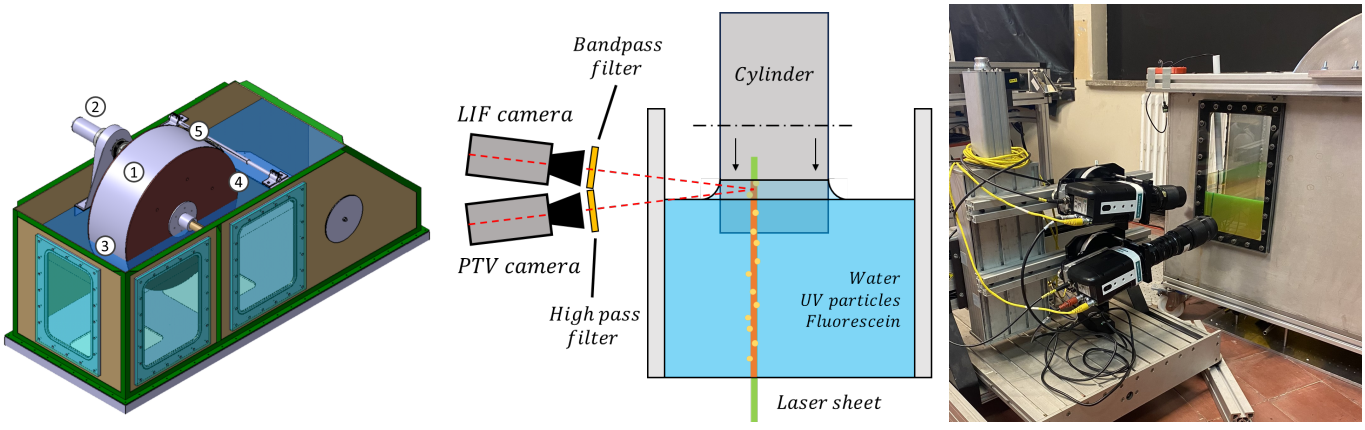

(a) (b) (c)

Figure 3. (a) View of the VKI MINERVA facility reproducing the dynamic wetting conditions. (b) View of the operating principle of LIF-PTV measurement. (c) Picture of the camera arrangement for the simultaneous acquisition of the interface and the velocity field.

The facility is equipped with various windows for optical access. The experimental setup consists of two high-speed cameras (Phantom SpeedSense M310 with 1280×800 pixel resolution) placed above and below the interface as shown in Figure 3b. These cameras are used, respectively, to capture the interface, and to perform PTV within the liquid. The LIF camera is equipped with a Vivitar 70-150 mm lens combined with 27.5 mm of extension tubes, providing a field of view of $65.4 \times 40.9\ \mathrm{mm}$ at full resolution. The PTV camera is equipped with a Nikon AF Nikkor 70-210 mm with 68 mm of extension tubes, resulting in a field of view of $34.4 \times 21.5\ \mathrm{mm}$.

The interface is detected by inducing fluorescence of the fluorescein present in the liquid. As a result, the difference in light intensity between the liquid and the gas phase makes edge detection easier. The illumination is carried out by a Quantronix Darwin Duo laser, exciting the colorant at a wavelength of 527 nm, which in turn emits light at 515 nm. The laser sheet has a thickness of around one millimeter and enters through a visualization window at the bottom of the bath to avoid direct interference with the interface.

Regarding the velocimetry, Particle Tracking Velocimetry (PTV) was preferred over traditional correlation-based velocimetry to avoid spatial modulation and, thus, better handle the large gradients encountered in this configuration. The seeding was carried out using neutrally buoyant fluorescent particles (UVPMS-BR 53-63 µm, 0.995 $\mathrm{g/cm^3}$). The particles, exited with the same laser sheet, emit light at a wavelength of 607 nm. The difference in wavelength between the laser, fluorescent emission by the fluorescein, and fluorescent emission by the particles allows to perform both LIF and PTV simultaneously. Each camera is equipped with optical filters (LIF: 580 nm high-pass, PTV: $514.5 \pm 5\ \mathrm{nm}$ band-pass), to limit the image acquisition to the relevant portion of the spectra. A picture of the experimental setup is presented in Figure 3c.

3.2. Image processing for interface tracking and velocimetry

An example of images acquired by the LIF camera is shown in Figure 4a. The first step of the processing consists of detecting the cylinder wall using gradient-based edge detection on a different set of images acquired without optic filters. The points identified on the cylinder wall are fitted with a circle equation, allowing to retrieve the entering angle θ_e function of the contact line position. The same approach is used to detect all the points forming the interface. These points are fitted with a support vector regression (SVR), resulting in a smooth interface ($\tilde{h} = f(x)$) shown in Figure 4c, from which the contact angle θ is computed as follows:

$$\theta = \pi - \theta_e - \tan^{-1}\left(\frac{d\tilde{h}}{dx}\Big|_{wall}\right). \tag{2}$$

From the images acquired by the PTV camera (Figure 4b), the velocity field is extracted using the open-source Python code $Tractrac$ (Heyman, 2019). The code is designed to compute the position,

velocity, and acceleration of the particles based on time-resolved images. The next particle position is identified using the information on the previous frames, the next particle position is estimated and then corrected.

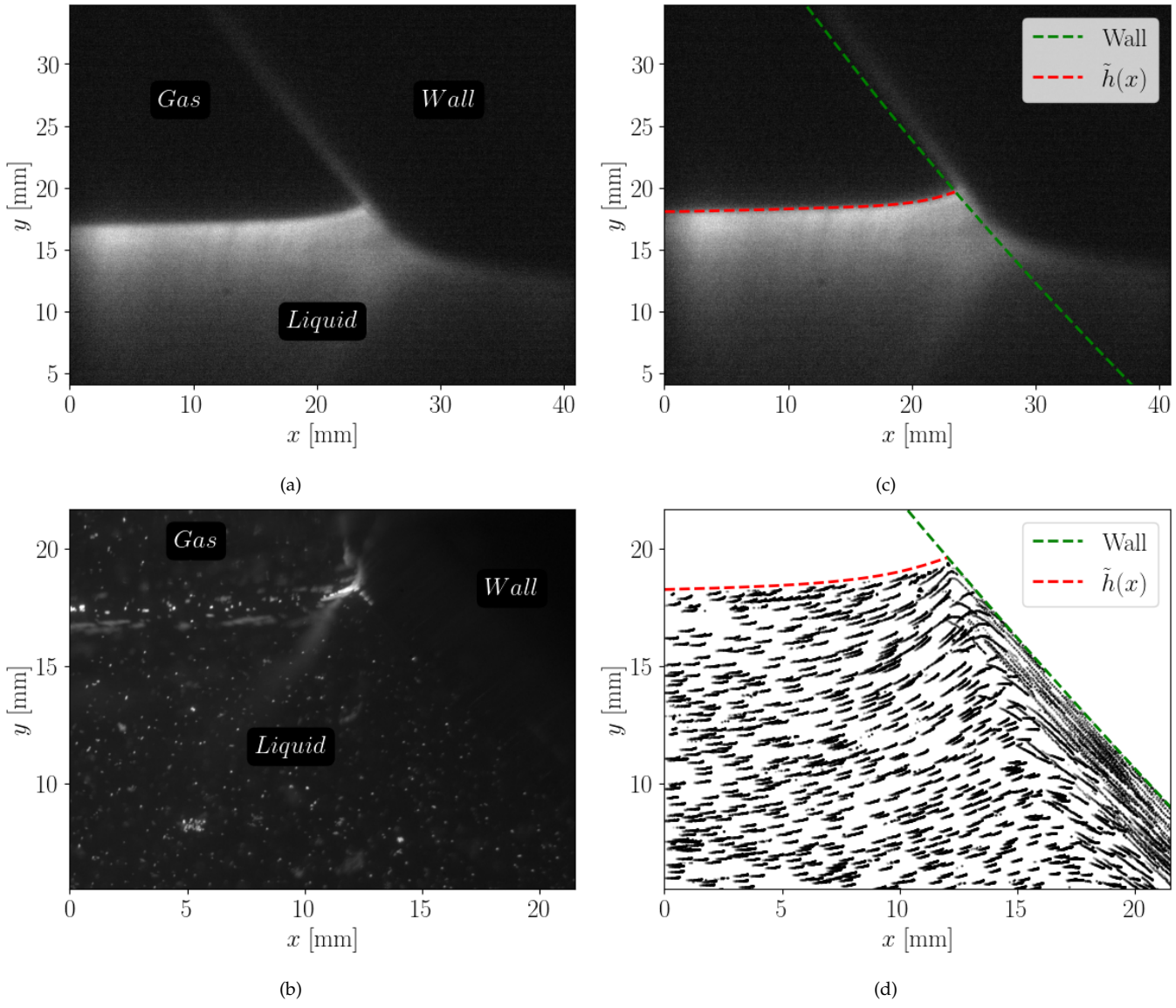

Figure 4. Images acquired by (a) the LIF camera and (b) the PTV camera. (c) Interface $\hat{h}(x)$ and wall extracted from the LIF measurement. (d) Particle paths reconstructed with Tractrac code over 20 timesteps, bounded by the LIF measurements.

A calibration between the two cameras is carried out to define a common reference frame for the two measurement techniques. This also allows the interface measurements to remove particle reflection at the interface and the wall for the PTV analysis. The calibration procedure is illustrated in Figure 5. The interface detected in the LIF reference frame (Figure 4c), is transferred into the PTV reference frame (Figure 4d). Using a dotted plate, the calibration correct for the scaling factor and

the shift between the two cameras.

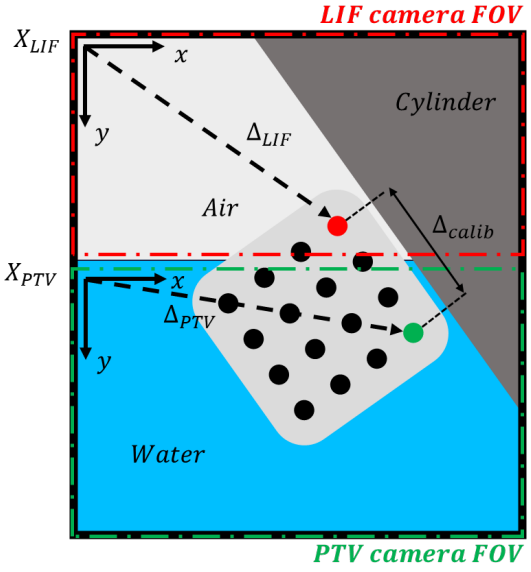

Figure 5. Calibration of two cameras through a liquid-gas interface.

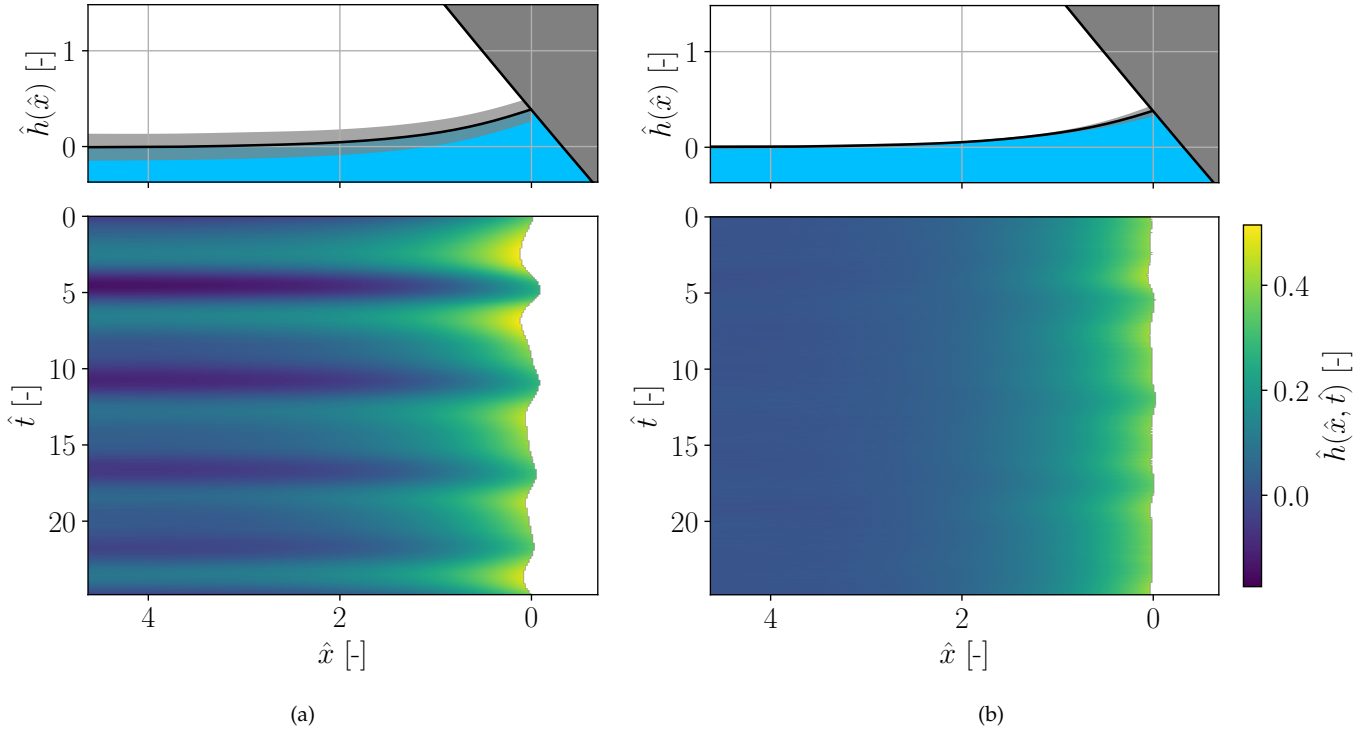

Figure 6. Interface dynamics: (a) as measured and (b) with the correction based on the POD. The average interface shape is surrounded by its maximum displacement in grey (top). The spatiotemporal evolution of the interface $\hat{h}$ is presented as a function of the dimensionless coordinate $\hat{x}$ and the dimensionless time $\hat{t}$ (bottom).

3.3. Modal decomposition and velocity field assimilation

In order to analyze the dynamic of the interface, the detection is performed on a complete image set (4000 frames). Figure 6 presents the spatiotemporal evolution of the interface, as a function of the dimensionless triple point distance $\hat{x} = x/l_c$, and the dimensionless time $\hat{t} = tl_c/u_p$. The average interface shape is shown on top and is surrounded in grey by the maximal displacement. It can be seen from Figure 6a that waves present in the bath are impacting the interface with a relatively large amplitude. To observe and characterize the impact of the entering velocity, a POD of the interface is carried out using the open-source $Modulo$ Python package (Poletti et al., 2023). The POD divides the interface dynamic into (1) the strong solid motion of the interface due to the waves and (2) the interface deformation. The corrected interface is obtained by subtracting the vertical motion of the waves from the original interface. The x coordinates are re-adjusted such that the last point of the interface remains on the wall. The result is shown in Figure 6b, where the triple point motion is only induced by the deformation of the interface and no longer by its elevation due to the waves.

The same correction is applied to the PTV results, for the particle coordinates $\mathbf{X} = (\mathbf{x}, \mathbf{y})$ but also on their velocity information $\mathbf{U} = (\mathbf{u}, \mathbf{v})$, involving the temporal derivatives of the wave fluctuations.

From the point-wise information of PTV measurement, we extract a smooth and continuous form of the velocity field through data assimilation. More precisely, the radial basis functions framework (RBF) is used to obtain an analytical form of the velocity field. Following Sperotto et al. (2022), the RBF regression can be assembled taking into account constraints that must be respected by the assimilated fields. We use two different constraints: a solenoidal flow and the kinematic boundary condition. This constraint ensures that the gas-liquid interface is deformable but continuousKalliadasis et al. (2012).

The scattered velocity information is approximated by a number n_b of radial basis ϕ_r, each with an associated weight w_r. The value of these functions only depends on a shape factor c, and on the radial distance between the collocation point of the basis $\mathbf{x}_c = (x_c, y_c)$ and the considered point $\mathbf{x} = (x, y)$. We use C4 basis, defined as:

$$\phi_r = \begin{cases} (1 + d(\mathbf{x})/c_r)^5 \, (1 - d(\mathbf{x})/c_r)^5 & |\mathbf{d}| \leq c_r \\ 0 & |\mathbf{d}| > c_r \end{cases} \tag{3}$$

with $\mathbf{d} = \mathbf{x}_c - \mathbf{x}$.

The values of the weights w_r are obtained by minimizing the square difference between the regression and the measurement. The approximated solution of $\mathbf{U}$, denoted $\tilde{\mathbf{U}}$ is then obtained by combining all the bases with their associated weight. This operation is achieved in one matrix multiplication

$$\mathbf{U}(\mathbf{X}) \approx \tilde{\mathbf{U}}(\mathbf{X}) = \sum_{r=1}^{n_b} \phi_r(\mathbf{X}) w_r = \mathbf{\Phi}(\mathbf{X})\mathbf{w} \tag{4}$$

where $\mathbf{\Phi}$ is the matrix containing all the bases and $\mathbf{w}$ is the weight vector. Concerning the constraints, these are implemented in the form of Lagrangian multipliers in the cost function. In the first instance, we want to enforce $\nabla \cdot \tilde{\mathbf{U}} = 0$ since we can assume the flow to be 2D and incompressible. The constraint, applied on the set of point $\mathbf{X}_\nabla$ is written as:

$$\nabla \cdot \mathbf{U} = \frac{\partial \mathbf{u}}{\partial x} + \frac{\partial \mathbf{v}}{\partial y} = 0 \qquad \rightarrow \qquad \nabla \cdot \tilde{\mathbf{U}} = \frac{\partial \mathbf{\Phi}_u(\mathbf{X}_\nabla)}{\partial x}\mathbf{w}_u + \frac{\partial \mathbf{\Phi}_v(\mathbf{X}_\nabla)}{\partial y}\mathbf{w}_v = 0. \tag{5}$$

Similarly, the kinematic boundary condition which relates the velocity field to the interface dynamic is implemented, on the set of point $\mathbf{X}_I$ as follows:

$$\mathbf{v} = \frac{\partial h}{\partial t} + \mathbf{u}\frac{\partial h}{\partial x} \qquad \rightarrow \qquad \mathbf{\Phi}_v(\mathbf{X}_I)\mathbf{w}_v = \frac{\partial h}{\partial t} + \mathbf{\Phi}_u(\mathbf{X}_I)\mathbf{w}_u\frac{\partial h}{\partial x}. \tag{6}$$

where $\partial h/\partial t$ is the temporal evolution of the interface while $\partial h/\partial x$ is the interface slope and are both extracted from the LIF measurement.

In practice, the regression is performed using the Spicy Python library (Sperotto et al., 2024), which includes a complete and optimized version of the method described above. The divergence-free constraint is already available while the kinematic boundary condition has been added. Moreover, the partition of unity method was used as in Ratz & Mendez (2024) to considerably reduce the computation time of the regression.

4. Results

The average interface shape is extracted from the corrected interface evolution (Figure 6b), and is plotted in Figure 7a for different Weber numbers through different entering velocities u_p. The case at We = 0 corresponds to the static case, where the interface shape is a solution of the Young-Laplace equation, since only capillarity and gravity act on the interface. In this condition, the static contact angle is measured between the interface and the wall inclined of $\theta_e = 49°$. The difference between the dynamic contact angle θ_d and the static contact angle $\theta_s = 84°$ is shown in figure Figure 7b, with the error bar accounting for the fluctuation in time. As the substrate velocity u_p increases, the triple point is pushed downward due to viscous forces, resulting in different interface shapes. The plate motion induced a strong decrease in the liquid level while the interface tends toward an asymptotic flat shape, where a further increase in Weber number has less and less impact. The visco-capillary theory predicts the contact angle to increase monotonously with u_p until $\theta = 180°$ (hence the interface is parallel to the wall). This trend is indeed observed for low

Weber numbers but is lost after We ≈ 10, where the contact angle experiences a slight reduction before increasing again following a different trend.

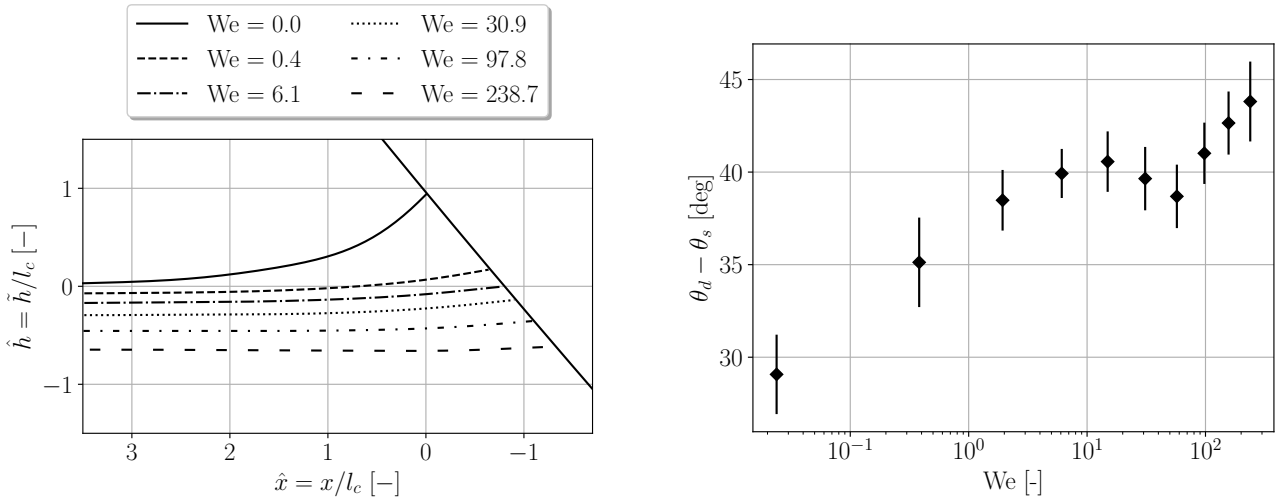

(a) (b)

Figure 7. Impact of the Weber number on (a) the interface shape and (b) the difference between the dynamic θ_d and the static θ_s contact angle, for an entering angle $\theta_e = 49°$ and $\theta_s = 84°$.

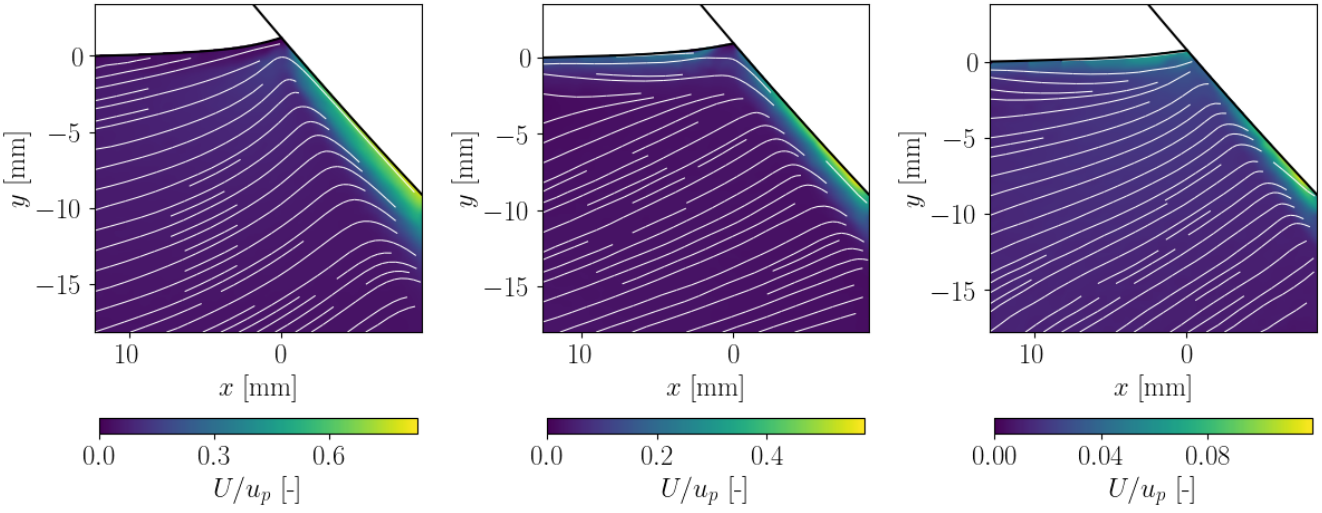

(a) (b) (c)

Figure 8. Average velocity field at (a) We = 0.024, $u_p = 0.025$ m/s, (b) We = 0.38, $u_p = 0.1$ m/s, and (c) We = 6.1, $u_p = 0.4$ m/s, obtained with the physically constraint RBF assimilation.

We first analyze the velocity using the average flow, derived from the RBF assimilation of a complete set of images (4000 frames). The results are shown in Figure 8, for $u_p = 0.025$ m/s, $u_p = 0.1$ m/s and $u_p = 0.4$ m/s. These conditions are sufficiently steady for the average velocity field to be representative of the entire measurement. In Figure 8a, the Weber number is small enough to consider

the flow to be in the viscous regime. The plate motion induces uniform and large-scale motion of the fluid toward the wall. The flow undergoes a curvature that becomes more pronounced as we approach the triple point, caused by the two different boundary conditions the flow must respect. As the entering velocity is increased (Figure 8b and Figure 8c), the boundary layer thickness is reduced, and consequently, the number of measurement points within it, as shown by the maximum value of U/u_p. An interesting observation is the development of an interface velocity starting from We = 0.38, with a magnitude larger than the bulk velocity. Apart from a local velocity pattern near the interface, induced by this interface velocity, the general flow appears qualitatively close to the creeping flow solutions described in Huh & Scriven (1971), especially for the case of the modulated wedge solution, accounting for the curvature of the interface as presented in Gupta et al. (2023).

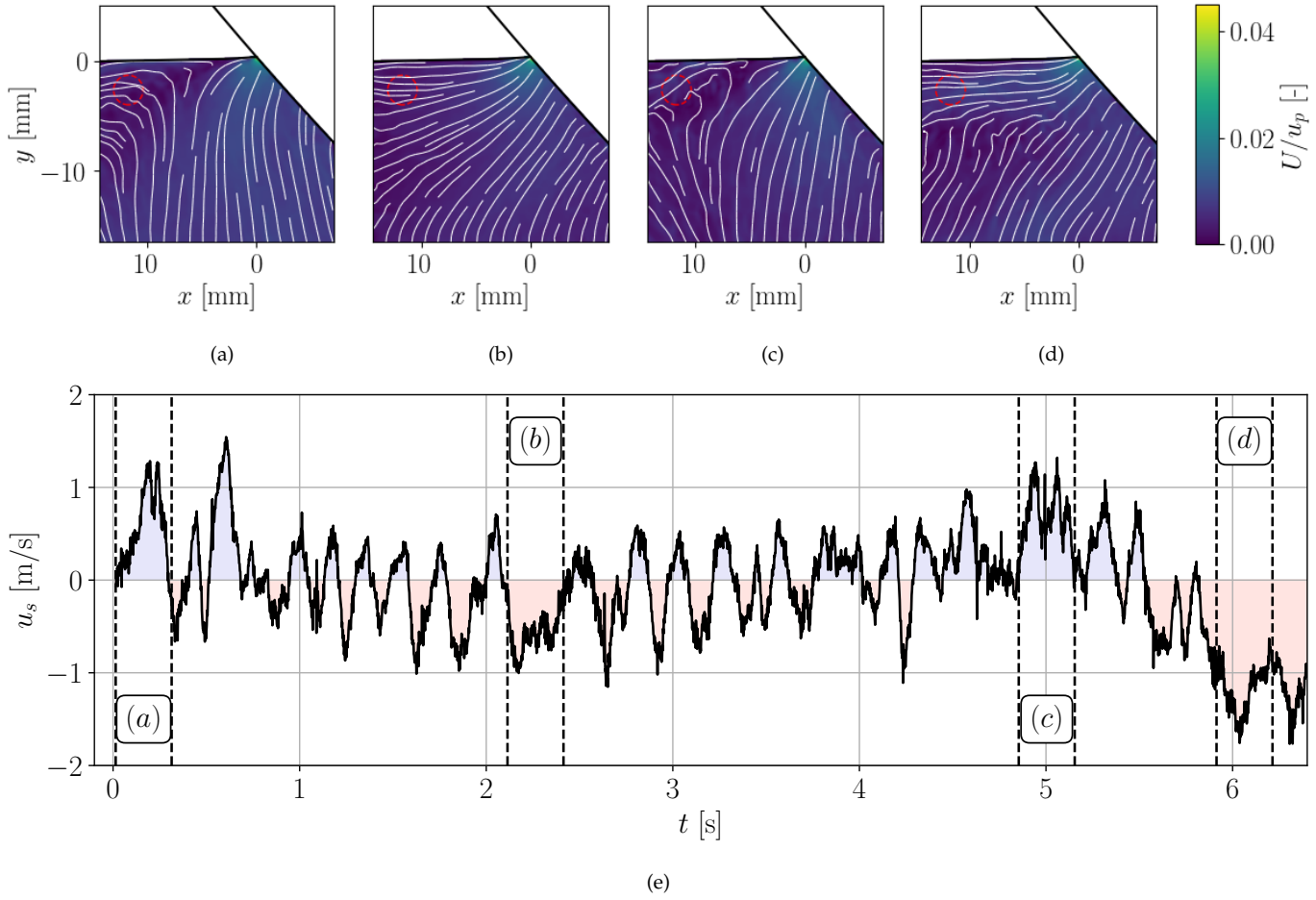

Figure 9. (a-d) Velocity field for u_p = 2.5 m/s, We = 235, Ca = 0.038, at different time steps, revealing the different unsteady flow patterns near the contact line. (e) Time evolution of the horizontal velocity u_s in the splitting region (red circle). The negative (in red) and positive (in blue) values correspond respectively to a flow moving towards and away from the wall.

As soon as the entering velocity and the inertia become large ($u_p \geq 0.9\mathrm{m/s}$, that is We ≥ 30), large-scale motions in the bath cause the flow to become unsteady and result in different patterns. These are analyzed separately by performing multiple sub-regressions on different subsets of images

(150 frames) in which the flow maintains one single pattern. Several of these periodic patterns are documented in Figure 9 (a)-(d). Figure 9e shows the time evolution of the horizontal velocity in the splitting region u_s (red circle in Figure 9 (a)-(d)) where the negative (red) and the positive (blue) values, respectively correspond to a flow going, toward and away from the wall. We present the case of $u_p = 2.5\mathrm{m/s}$ (We = 235), where the different patterns are most visible. The periods considered for the velocity fields regression are indicated by the dashed lines in figure Figure 9e. The flows in cases (a) and (d) are similar to those observed under viscous conditions (We < 30). However, in cases (a) and (d), we observe a different flow pattern, almost vertical and splitting near the interface. The flow field topology changes at a relatively large timescale ($\approx 0.2Hz$) compared to the interface fluctuations ($\approx 5Hz$), whose footprint can be observed on u_s. At such large Weber numbers, the velocity field starts to have a dependence on the geometry of the facility, and on the large-scale motion of the fluid in the surrounding region.

5. Conclusions

This work investigated dynamic wetting occurring when a substrate enters a bath at a large velocity, leading to Weber numbers of the order of $\sim \mathcal{O}(10^2)$. The gas-liquid interface dynamics in these conditions are dominated by inertia and have never been investigated in such detail before. We present a brief dimensionless analysis to relate the investigated conditions to those of modern hot dip galvanizing lines, where the stability of the contact line plays a crucial role in producing defect-free coated products. The experimental analysis combined laser-induced fluorescence and image processing-based interface tracking with particle tracking velocimetry measurements within the liquid films. The evolution of the interface shape and the dynamic contact angle was investigated over a wide range of Weber numbers and complemented by the velocity field.

We highlighted a region of critical Weber number (We = 10), below which the contact angle evolution is monotonous, in agreement with the viscous theories. Above this value, the evolution becomes non-linear. The analysis of the velocity field reveals that the flow remains steady up to We = 30. For We < 30, the observed flow is qualitatively close to the viscous models. At larger Weber numbers, we observed an unsteady flow that oscillates between a 'viscous-like' flow and a splitting flow. The time scale involved in the flow field oscillation appeared different from the one of the interface displacement.

The proximity between the critical We number of the interface and the critical We number of the velocity field suggests that the two behaviors are linked. Ongoing work aims at clarifying how the velocity field impacts the interface shape and, consequently, the dynamic contact angle.

References

Benkreira, H. (2004). The effect of substrate roughness on air entrainment in dip coating. *Chemical Engineering Science*, *59*(13), 2745–2751. doi: 10.1016/j.ces.2004.03.024

Bormashenko, E. Y. (2013).
In *Wetting of real surfaces* (pp. 78–91). De Gruyter. doi: 10.1515/9783110258790.78

Burley, R., & Kennedy, B. (1976). An experimental study of air entrainment at a solid/liquid/gas interface. *Chemical Engineering Science*, *31*(10), 901–911. doi: 10.1016/0009-2509(76)87040-6

Chen, Q., Ramé, E., & Garoff, S. (1997). The velocity field near moving contact lines. *Journal of Fluid Mechanics*, *337*, 49–66. doi: 10.1017/s0022112096004806

Dussan V., E. B., Ramé, E., & Garoff, S. (1991). On identifying the appropriate boundary conditions at a moving contact line: an experimental investigation. *Journal of Fluid Mechanics*, *230*, 97–116. doi: 10.1017/s0022112091000721

Fell, D., Auernhammer, G., Bonaccurso, E., Liu, C., Sokuler, R., & Butt, H.-J. (2011). Influence of surfactant concentration and background salt on forced dynamic wetting and dewetting. *Langmuir*, *27*(6), 2112–2117. doi: 10.1021/la104675t

Fricke, M., & Bothe, D. (2020). Boundary conditions for dynamic wetting - a mathematical analysis. *The European Physical Journal Special Topics*, *229*(10), 1849–1865. doi: 10.1140/epjst/e2020-900249-7

Fuentes, J., & Cerro, R. L. (2005). Flow patterns and interfacial velocities near a moving contact line. *Experiments in Fluids*, *38*(4), 503–510. doi: 10.1007/s00348-005-0941-4

Gupta, C., Choudhury, A., Chandrala, L. D., & Dixit, H. N. (2023). An experimental study of flow near an advancing contact line: a rigorous test of theoretical models. *Under consideration for publication in J. Fluid Mech.*.

Heyman, J. (2019). Tractrac: A fast multi-object tracking algorithm for motion estimation. *Computers & Geosciences*, *128*, 11–18. doi: 10.1016/j.cageo.2019.03.007

Huh, C., & Scriven, L. (1971). Hydrodynamic model of steady movement of a solid/liquid/fluid contact line. *Journal of Colloid and Interface Science*, *35*(1), 85–101. doi: 10.1016/0021-9797(71)90188-3

Kalliadasis, S., Ruyer-Quil, C., Scheid, B., & Velarde, M. G. (2012). *Falling liquid films*. Springer London. doi: 10.1007/978-1-84882-367-9

Kistler, S. F., & Schweizer, P. M. (1997). Coating science and technology: An overview. In *Liquid film coating* (pp. 3–15). Springer Netherlands. doi: 10.1007/978-94-011-5342-3_1

Landau, L., & Levich, B. (1988). Dragging of a liquid by a moving plate. In *Dynamics of curved fronts* (pp. 141–153). Elsevier. doi: 10.1016/b978-0-08-092523-3.50016-2

Mayer, H. C., & Krechetnikov, R. (2012). Landau-levich flow visualization: Revealing the flow topology responsible for the film thickening phenomena. *Physics of Fluids*, *24*(5). doi: 10.1063/1.4703924

Mitra, S., & Evans, G. (2018). Dynamic surface wetting and heat transfer in a droplet-particle system of less than unity size ratio. *Frontiers in Chemistry*, *6*. doi: 10.3389/fchem.2018.00259

Mohammad Karim, A., & Kavehpour, H. P. (2018). Effect of viscous force on dynamic contact angle measurement using wilhelmy plate method. *Colloids and Surfaces A: Physicochemical and Engineering Aspects*, *548*, 54–60. doi: 10.1016/j.colsurfa.2018.03.058

Poletti, R., Schena, L., Ninni, D., & Mendez, M. A. (2023). MODULO: a python toolbox for data-driven modal decomposition. *submitted to Journal of Open Sofwares (JOSS)*.

Quetzeri-Santiago, M. A., Castrejón-Pita, A. A., & Castrejón-Pita, J. R. (2019). The effect of surface roughness on the contact line and splashing dynamics of impacting droplets. *Scientific Reports*, *9*(1). doi: 10.1038/s41598-019-51490-5

Quéré, D. (1999). Fluid coating on a fiber. *Annual Review of Fluid Mechanics*, *31*(1), 347–384. doi: 10.1146/annurev.fluid.31.1.347

Ramé, E., & Garoff, S. (1996). Microscopic and macroscopic dynamic interface shapes and the interpretation of dynamic contact angles. *Journal of Colloid and Interface Science*, *177*(1), 234–244. doi: 10.1006/jcis.1996.0026

Ratz, M., & Mendez, M. A. (2024). A meshless and binless approach to compute statistics in 3d ensemble ptv.
doi: 10.48550/ARXIV.2403.11828

Snoeijer, J. H., Ziegler, J., Andreotti, B., Fermigier, M., & Eggers, J. (2008). Thick films of viscous fluid coating a plate withdrawn from a liquid reservoir. *Physical Review Letters*, *100*(24), 244502. doi: 10.1103/physrevlett.100.244502

Sperotto, P., Pieraccini, S., & Mendez, M. A. (2022, June). A meshless method to compute pressure fields from image velocimetry. *Measurement Science and Technology*, *33*(9), 094005. doi: 10.1088/1361-6501/ac70a9

Sperotto, P., Ratz, M., & Mendez, M. A. (2024). SPICY: a Python toolbox for meshless assimilation from image velocimetry using radial basis functions. *Journal of Open Source Software*, *9*(93). doi: 10.21105/joss.05749

Zhao, Y. (2014). Moving contact line problem: Advances and perspectives. *Theoretical and Applied Mechanics Letters*, *4*(3), 034002. doi: 10.1063/2.1403402